Journal Name

ARTICLE

High-rate capability and superior cyclability of flower-like Sb$_2$S$_3$ anode for high capacity sodium-ion batteries

Yaoyao Zhu, Ping Nie, Laifa Shen, Shengyang Dong, Qi Sheng, Hongsen Li, Haifeng Luo, Xiaogang Zhang*

Flower-like Sb$_2$S$_3$ has been prepared through a simple and facile polyol refluxing process. When tested as an anode for sodium-ion batteries, the material delivers high reversible capacity of 835.3 mAh g^{-1} at 50 mA g^{-1} after 50 cycles, and maintains a capacity of 641.7 mAh g^{-1} at 200 mA g^{-1} after 100 cycles. Even up to 2000 mA g^{-1}, a capacity of 553.1 mAh g^{-1} can be obtained, indicating excellent cycle performance and superior rate capability. Furthermore, we have investigated the formation mechanism of the micro-flowers. The additive facilitates controlled-release of reactant to form uniform and shaped nanosheets, optimal reaction time makes for nanosheets self-assembled into microflowers.

Introduction

Recent years, widely application of Li-ion batteries in portable devices results in expanding use of it. However, the lithium-rich resources are finite on the earth[1]. Considering the potential advantages of low cost and widespread availability of sodium resources[2]. Also, from the electrochemical point of view, sodium possesses a very negative redox potential (-2.71V, vs. SHE), which makes it the most advantageous for battery applications after lithium[1, 3]. Room-temperature sodium-ion batteries attract increasing attention for large scale energy storage applications in renewable energy and smart grid, which required low cost, high safety, cycle stability[4-10].

It is well known that the comprehensive performance of the batteries relates to electrode materials, electrolyte and the compatibility of them. Great efforts have been made to improve Na-ion storage properties[1, 11, 12]. Nevertheless, recent researches mainly focused on positive electrode materials[3], several works devoted to the negative ones[1, 2, 13-15] and the primary candidates are the materials that can alloy and de-alloy with sodium in a reversible manner[2, 14, 16-18]. Compared with carbon-based anode materials[19], some metals or alloy materials yield a much higher specific capacity via a alloying/de-alloying mechanism[20-25]. However, for these anode materials, severe structural degradation due to large volume expansion leads to loss of electric contact within the electrodes and considerable performance fading[26-29]. There are two efficient strategies to overcome the adverse effects associated with such degradation. On the one hand, nanoparticles supported by carbon matrices have been designed[25, 30-32], for another, composites with inactive elements buffering the volume expansion[33-35]. Qian et al.[36] demonstrated that a kind of Sb/C nanocomposite with a reversible 3 Na storage capacity of 610 mAh g^{-1}, a superior rate capability at a very high current of 2000 mA g^{-1} and a long-

term cycling stability with 94% capacity retention over 100 cycles. Baggetto et al.[33] reported for the first time that FeSb$_2$ as anode for sodium-ion batteries, the reversible storage capacity amounts to 360 mAh g^{-1}. Previous work by Denis et al.[37] investigated the use of Sb$_2$S$_3$ nanoparticles decorated graphene composite as anode for sodium-ion batteries. Theoretically one mole of Sb$_2$S$_3$ can get 12 moles of electrons and Na-ion resulting in a theoretical capacity of 946 mAh g^{-1}. The advantages of Sb$_2$S$_3$ for Na-ion batteries are listed as follows. Firstly, Sb$_2$S$_3$ possessed higher theoretical capacity than Sb (660 mAh g^{-1}) because of lower weight of the S atoms. Secondly, sulphur provide with a mechanical buffering of volume change during charge and discharge. Third, sulphides formation is typically more reversible than oxides. Recent studies focus on the combination of Sb$_2$S$_3$ with carbon based materials. While nanostructured electrode materials have attracted much attention because of improved kinetic performance by reducing the transport length of sodium ions and electrons as well as bearing the volume change[38, 39].

Herein a flower-like Sb$_2$S$_3$ was constructed in a simple and mild method, which achieved high capacity, good rate capability and excellent cycling performance. Further investigation was performed on the growth mechanism of the crystalline metal sulphides. In our research, we have developed a facile polylol refluxing process to prepare Sb$_2$S$_3$ microflowers. The material behaves extremely well as the anode for NIB. About 10.6 Na (835.3 mAh g^{-1}) can be reversibly alloy and de-alloy from the material at a rate of 50 mA g^{-1} (about 0.05C) without any capacity fading after 50 cycles at this current density. After 100 cycles at the current rate increased to 200 mA g^{-1}, a capacity of 641.7 mAh g^{-1} can be obtained. In addition to the stable cycle performance, the material also shows excellent rate capability. When the current rate increased to 2000 mA g^{-1}, 72% of the capacity (553.1 mAh

g^{-1}) can still be remained, corresponding to the charge and discharge time of 28 min. It would be allowed for fast charging of NIBs in the future. The enhanced rate capability and cycle stability are attributed to the novel structure of nanosheets self-assembled micro-flowers. Fast rate capability owing to the shorten paths for Na-ion and electrons diffusion[40] and stable cycling behaviour can be attributed to accommodating the strain generated during cycling.

Experimental

Materials Synthesis

All of the reactants and solvents were of analytical grade and used without further purification. Sb_2S_3 nanostructures were prepared *via* a facile polyol refluxing process. To get Sb_2S_3 micro-flowers, 3 mmol antimony trichloride and 2.5 mmol L-cysteine were mixed with 60 mL EG solution in presence of 6 mL ethylenediamine. The refluxing system was kept at 175 °C for 50 minutes. After cooled down to ambient temperature naturally, the resulted precipitation was collected by centrifugation and washed thoroughly with water and ethanol several times, vacuum dried at 80 °C overnight for characterizations. We have prepared comparable samples in a similar procedure to that described above, instead, the reaction time was reduced to 10 min, 20 min, 30 min, 40 min. The other one is in absence of ethylenediamine.

Materials Characterization

The morphologies and structure of products were characterized by field-emission scanning electron microscopy (FESEM, LEO 1430VP, Germany). Transmission electron microscopy (TEM) images were recorded using a HRTEM (JEOL JEM-2010). The composition of the samples was analyzed using an energy dispersive X-ray spectrometer (EDS) attached to the SEM instrument. The powder X-ray diffraction (XRD) pattern was collected on a Bruker D8 Advance diffractometer equipped with Cu Kα radiation over the 2θ range of 10-70°. The adsorption–desorption isotherms of nitrogen were measured by using automatic volumetric adsorption equipments (BELSORP mini II, BEL Japan, Inc.) and specific surface areas were calculated by non-localized density functional theory (NLDFT) using N_2-adsorption isotherms at 77 K.

Electrochemical Measurements

Electrodes made by mixing active materials with acetylene black and carboxymethyl cellulose (CMC) sodium salt in de-ionized water in ratio of 3:1:1. The electrode was fabricated using 2032 coin cells with sodium metal as counter electrode. One molar $NaClO_4$ in propylene carbonate with 5 wt% fluorinated ethylene carbonate (FEC) was used as the electrolyte. The glass microfiber filters (GF/D Whatman) served as the separator. Galvanostatic charge/discharge cycles were performed on a LAND 2001A Battery Tester between 0.01 and 2.00 V at various current densities. Cyclic voltammetry measurements were carried out on an electrochemical workstation (CHI750D) in the potential range of 0.01-2.00 V *vs.* Na$^+$/Na at a scan rate of 0.1 mV s^{-1}.

Results and discussion
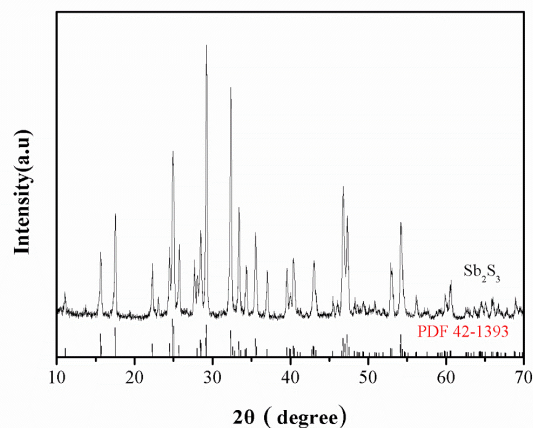
Fig. 1 XRD pattern of Sb_2S_3.

The crystallographic structure of the sample was characterized by means of XRD (Fig. 1). It demonstrated a series narrow and shape diffraction peaks in range of 10-70° (middle curve), all of which matches well with stibnite structure (JCPDS No. 42-1393), evidencing the high crystallinity of orthorhombic phase with lattice constants a = 1.124 nm, b = 1.131 nm, and c = 0.384 nm. No additional diffraction peak from impurities is detected, indicating high purity of Sb_2S_3.
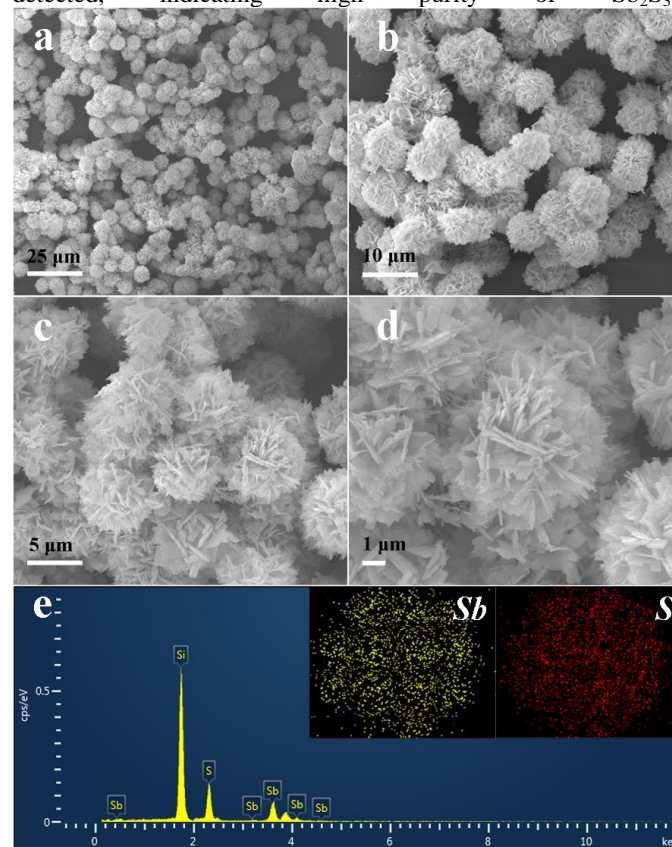
Fig. 2 a-d) FESEM and e) EDS images of Sb_2S_3.

The morphologies and microstructures of the synthesized Sb_2S_3 were characterized by SEM and TEM. The low

magnified panoramic SEM image proved the formation of a large number of stereoscopic flower-like Sb_2S_3 with average diameter about 7-10 μm, piling up of those flower-like Sb_2S_3 remains abounding space rather than aggregating into bulks(Fig. 2a, b). Fig. 2c, d clearly exhibits that Sb_2S_3 flowers are built from dozens of nanosheets with thickness of 50 nm. Nanosheets are extended radially from the center point and formed sphere shaped flowers. The irregular stacking of nanosheets results in abundant slits and holes on the surface and it is reasoned to infer that the interior of micro-flowers may remain plentiful of interspace. In addition, we studied the elemental distribution of the flower-like architecture material using energy-dispersive X-ray spectroscopy (EDX)-SEM mapping. As can be seen in Fig 2e, both sulphur (red) and antimony (yellow) well-distributed in the microstructures without any aggregation, which further clarified the synthesis of Sb_2S_3. What's more, both of the elements mapping could draw well the contour of a micro-flower.
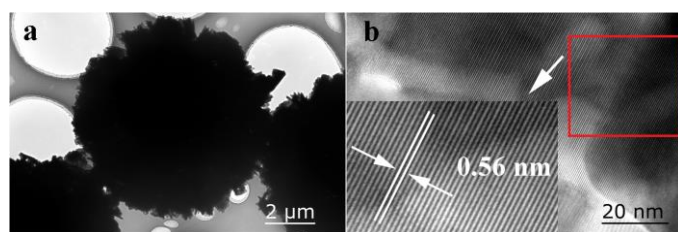

Fig. 3 a, b,) TEM images micro-flower Sb_2S_3.

Transmission electron microscopy (TEM) was further used to investigate microstructures and crystalline information of Sb_2S_3 micro-flowers (Fig 3a), which is in accordance with the SEM result. The average diameter of the as-prepared Sb_2S_3 flowers is about 7 μm. The micro-flowers are made up of individual nanosheets. The high resolution transmission electron microscopy (HRTEM) image in Fig. 3b reveals the Sb_2S_3 nanosheets, have smooth surface with high-crystalline in nature. In addition, a series of well-resolved parallel atomic planes that can be identified as the orthorhombic Sb_2S_3 planes with a d-spacing of 0.56 nm, well indexed to the (020) planes.

The N_2 adsorption-desorption isotherm of the Sb_2S_3 flowers (see ESI, Fig. S1) belongs to typical type Ⅱ isotherm with a H3 hysteresis loop. The rake radio of isotherms keeps increasing at the beginning manifests that the material is in absence of micropores and mesopores. The hysteresis loop occurs at the pressure of P/P_0=0.8, indicates the existence of narrow channels produced by nanosheets stacking. Brunauer–Emmett–Teller (BET) surface area of 22.787 m^2 g^{-1} is attributed to the surface area of self-assembled nanosheets.

A series of experiments were conducted to have an insight on the mechanism of formation of micro-flowers. In general, the final shape of nano-crystals was controlled by the inherent crystal structure during the initial nucleation stage and subsequent growth stage through the delicate control of external factors. Here we discussed the influence of external factors, such as the additive and reaction time[41.]
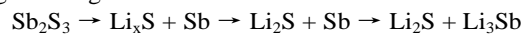
The morphology keeps changing alone with crystal growth, so we have a discussion about the influence of reaction time. According to the one variable principle, all of the reaction condition stay the same except reaction time, we designed comparable experiment group in 10, 20, 30, 40 min, respectively. As shown in Fig. S2, when the reaction time was controlled in 10 min (Fig. S2a), only disordered nanosheets accumulated into bulks can be found in the field of view. In 20 min (Fig. S2b), we can see some fluffy spheres which indicate

that nanosheets begin to self-assemble into particular shape. While the reaction time prolonged to 30 min (Fig. S2c), deformed micro-flowers are emerging in screen with numerous petal-like nanosheets clusters. When it is done by 40 min (Fig. S2d), initial shaping of micro-flowers appeared surrounding with dispersing nanosheets. Micro-flowers structure account for the majority as the polyol refluxing processing in 40 min. At the beginning of reaction, high concentrations of S^{2+} and Sb^{3+} result in fast growing of crystal, while the controlled-release of reactant to the benefit of formation of uniform and shaped nanosheets. Crystal growing slowed down as concentration of reactant decreased. Self-assemble of nanosheets into micro-flowers plays the leading role which could reduce the specific surface energy. Finally, we can come to a conclusion that in condition of polyol refluxing process, Sb_2S_3 crystals formed into nanosheet in prime stage, nanosheets self-assembled into micro-flowers with time extending, which is the well-known as Ostwald ripening process[42].
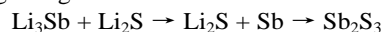
Beside the effect of reaction time, the additive of ethylenediamine makes a difference in the formation of flower-like structure. We performed an experiment without ethylenediamine, XRD was used to analyse the ingredients of the sample. All of the sharp peaks match well with PDF card of Sb_2S_3 (see ESI, Fig. S3). Without the addition of ethylenediamine, the Sb_2S_3 crystal would grow into bulks in several micrometers. Ethylenediamine is a kind of excellent chelating agent, served as bidentate ligand, antimony-ligand interaction could form chelate compound realized the controlled-release of antimony ions, which controlled the reaction rate of Sb_2S_3 immediately, the crystal growing into nanosheets instead of bulks. The slowing down production rate of Sb_2S_3 makes contribution to self-assemble of Sb_2S_3 nanosheets into micro-flowers structure as well.

Electrochemical properties of reversible Na alloying reaction with Sb_2S_3 composites have been demonstrated by recent researches, the theoretic capacity of Sb_2S_3 is 946 mAh g^{-1}, which is much more than carbon based materials. But the rate capability and cycling performance cannot meet the need of application. Motivated by the unique structural features, Sb_2S_3 micro-flowers are used as anode material for Na-ion batteries. Cyclic voltammetry at a scan rate of 0.1 mV s^{-1} over the potential window of 0.01-2.00 V vs. Na/Na^+ was carried out, the result is showed in Fig.4a. In the first scan, three peaks are observed at 0.35, 0.65 and 1.13 V for Sb_2S_3, corresponding to the electrochemical reduction reaction of Sb_2S_3 with Na and the formation of a solid electrolyte interphase (SEI). Peaks of the first scan are different from the subsequent both in location and intensity. Obviously the intensity of the reduction peaks in first cycle is stronger than the following ones, hinting that initial discharge capacity is larger than the succeeding ones. During subsequent scanning, Sb_2S_3 electrode shows reduction peaks around 0.2, 0.45 and 0.9V versus Na/Na^+ and oxidation peaks around 0.73 and 1.3V versus Na/Na^+. On the basis of similar mechanisms with metal alloying reaction with lithium:
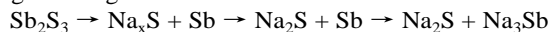
During discharge:
$$Sb_2S_3 \rightarrow Li_xS + Sb \rightarrow Li_2S + Sb \rightarrow Li_2S + Li_3Sb$$
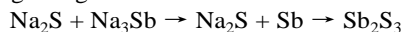During charge:
$$Li_3Sb + Li_2S \rightarrow Li_2S + Sb \rightarrow Sb_2S_3$$

There are two different phases during the insertion of Na^+, Sb_2S_3 first undergoes a conversion reaction between the sulphide and sodium, followed by a metal alloying reaction with sodium. The potential pair at 0.9/1.3V is attributed to conversion reaction with sulphur atoms in the material. The reduction and oxidation potential at 0.2/0.45 and 0.73V agree

well with the alloying reaction of Sb with Na. the reactions between Sb_2S_3 and sodium are expected as below:

During discharge:

$$Sb_2S_3 \rightarrow Na_xS + Sb \rightarrow Na_2S + Sb \rightarrow Na_2S + Na_3Sb$$

During charge:

$$Na_2S + Na_3Sb \rightarrow Na_2S + Sb \rightarrow Sb_2S_3$$

It is deserved to be mentioned that the reduction peaks are shifted to a lower potential at about 0.2V while the oxidation peaks exhibit little change in the first two cycles. But the reason is obscure so far, it may be the formation of SEI plays a role in promoting conductivity of interface that makes the difference, further studies needed to make it clear. The asymmetric voltage response upon charge and discharge is due to the growth of different interfaces, which induces different electrochemical equilibriums. This hysteresis voltage has been computed for conversional reactions and in accordance with experiments as demonstrated by Doublet et al[37].

Fig 4b shows the high-rate capability of Sb_2S_3. The electrode discharged and charged at a rate of 50, 100, 200, 500, 1,000, 2,000 mA g^{-1} for five cycles each. After the rate test, the electrode was tested again at 50 mA g^{-1} to investigate the effect of rate test on the stability of the electrode. The initial capacity at current rate of 50 mA g^{-1} is 729.6 mAh g^{-1}. A discharge capacity of 597.9 mAh g^{-1} can be obtained at a current rate of 1,000 mA g^{-1}, which corresponds to a charge and discharge time of about 57 min (1.06C). When the current rate increased to 2000 mA g^{-1} corresponds to a charge and discharge time of 28 min (2.11C), 76% of the capacity (554.6 mAh g^{-1}) can still be remained, sufficient for high-rate applications such as electric vehicles and power tools. The high-rate capability indicates fast transfer of Na and electrons through the special architecture. When the current rate reduced back to 50 mA g^{-1} after the rate test, the capacity actually bounced back to the initial value. Fig. 4c shows selected charge-discharge curves at different current rates. There is minimal increase in polarization even at high current rate of 2,000 mA g^{-1}. Compared with rGO/Sb_2S_3 reported before[41], our unique micro-flowers could be more efficient in decreasing polarization. The large specific surface area is more convenient for full contacting between anode materials and electrolyte, making a contribution to decrease of polarization. The sufficient contact providing short paths for electrons and sodium ions transfer.

In addition to the excellent rate capability, Sb_2S_3 also possesses good cycle stability. As shown in Fig. 4d, the cycle performance of Sb_2S_3 at a current rate of 50 mA g^{-1} shows a first discharge capacity of 970.2 mAh g^{-1} that is close to full utilization of the Sb_2S_3 active material with a Coulombic efficiency around 72.9%. Such a low efficiency of the first cycle was mainly attributed to the irreversible formation of the SEI film on the surface of the electrode during the first sodiation process. Capacity of Sb_2S_3 distinctly increases from 707 to 822 mAh g^{-1} during the first 10 cycles, which is due to extraction of Na-ion from the electrode that originally inserted during the first discharge. The Sb_2S_3 electrode exhibited excellent cycling performance, after 50 charge-discharge cycles under a current density of 50 mA g^{-1}, the Sb_2S_3 electrode still maintained an overall discharge capacity of 835.3 mAh g^{-1}. We have conducted further investigation on the cycling performance at current rate of 200 mA g^{-1} after 50 cycles at current density of 50 mA g^{-1}. When the current density increased to 200 mA g^{-1}, there is a sharp capacity decrease from 835.3 mAh g^{-1} to 682.7 mAh g^{-1}, and then the capacity maintain at a level of 641.7 mAh g^{-1} after 100 cycling. The unique flower-like structure anode materials possess great cycling

performance in Na-ion batteries even without embellished with carbon.
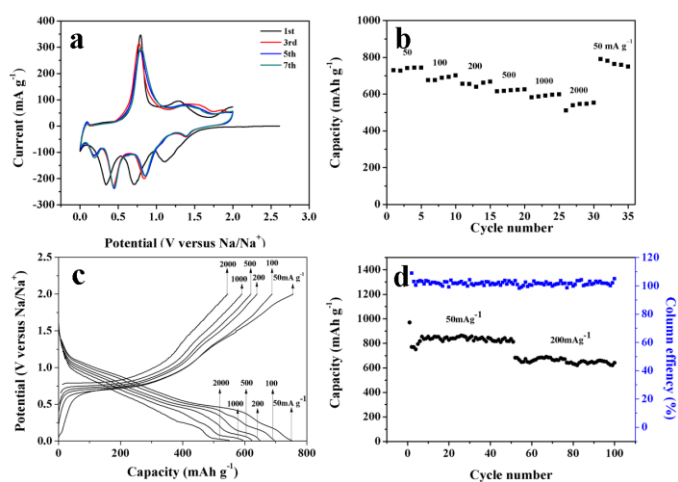
Fig. 4 a) Cyclic voltammograms of Sb_2S_3. b) Rate capability of the Sb_2S_3 electrode at various current rates from 50 mA g^{-1} to 2000 mA g^{-1}. c) Selected charge-discharge curves at different current rates. d) Cycle performance of Sb_2S_3 at current rate of 50 and 200 mA g^{-1}, respectively.

In contrast with superior electrochemical properties of flower-like Sb_2S_3, the performance of bulk Sb_2S_3 (without the addition of ethylenediamine) is much worse (see EIS, Fig. S4). Stereo architecture provides sufficient contact with electrolyte that improves the utilization of Sb_2S_3 and promotes diffusion of Na^+. Besides, it can also buffer the volume expansion of Sb during charge-discharge process.

In order to highlight the superior electrochemical performances of flower-like Sb_2S_3, we have made a comparison with published articles. As far as we know, there is only one report on Sb_2S_3 for NIB anode materials in the literature[37]. The comprehensive performance of our flower-like Sb_2S_3 is better than Sb_2S_3 NP@graphene. Both researches used the same electrolyte, which exclude the influence of electrolyte. The detailed indexes were listed in the Table 1.

Table 1 The comparison of electrochemical performance indexes of Sb_2S_3 NP@graphene and flower-like Sb_2S_3

Sample	Sb_2S_3 NP@graphene	flower-like Sb_2S_3
1ST cycle discharge capacity (mAh g^{-1})	845	970. 2
1ST cycle coulombic efficiency	69. 2%	72. 9%
Capacity of 50 cycles at 50 mA g^{-1} (mAh g^{-1})	670	835. 3
Capacity of 50 cycles at 200 mA g^{-1} (mAh g^{-1})	–	641. 7
Capacity at 2000 mA g^{-1} (mAh g^{-1})	560	554. 6

Further research on materials is crucial to cast light on the relationship between enhanced electrochemical performance and stable nanostructure. As shown in ESI, Fig. S5, well-distributes micro-flowers Sb_2S_3 wrapped with acetylene black adhered tightly to the collector. Nanosheets self-assembled flower-like structure was preserved well after milling, stacking of defined nanosheets created abundant slits and holes. After 20

cycles the uniform flower-like Sb_2S_3 displays negligible change except that the nanosheets become obscure because of the redox reaction, which demonstrates the unique puff structure promptly accommodates the volume change during short cycling (Fig. 5a, b). We also analyzed the elemental composition by EDS. After 20 cycles (see EIS, Fig. S6), the sample consists of antimony, sulphur, carbon and copper. Additionally, carbon is belonging to conductive additives and copper is belonging to collector.
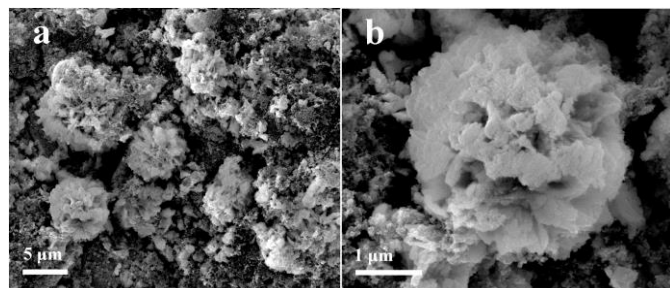
Fig. 5 a, b) SEM of Sb_2S_3 after 20 cycling at a current density of 50 mA g^{-1}.

Conclusions

In summary, we have demonstrated a facile strategy to fabricate flower-like Sb_2S_3. The reaction time in 50 min could produce uniform micro-flowers in addition of ethylenediamine based on the further study on the formation mechanism. The flower-like Sb_2S_3 exhibits much improved electrochemical properties as Na-ion battery anodes. Such improvement of the electrochemical performance should be attributed to unique structure of flower-like Sb_2S_3. We herein demonstrate that nanosheets self-assembled micro-flowers are beneficial structures not only mitigate volume expansion, but also provide effective diffusion pathways for electrons and sodium ions. What's more, compared with other processing, the synthetic method should be highlighted in this paper: low requirements for equipment, high efficiency, energy saving. It is a potential synthesis for industrialization in large scale.

Acknowledgements

Notes and references

Jiangsu Key Laboratory of Materials and Technology for Energy Conversion (MTEC), Key Laboratory for Intelligent Nano Materials and Devices of Ministry of Education, College of Material Science Engineering, Nanjing University of Aeronautics and Astronautics, Nanjing, China. E-mail: azhangxg@163.com; Fax: +86 025 52112626; Tel: +86 025 52112918

1. S.-W. Kim, D.-H. Seo, X. Ma, G. Ceder and K. Kang, Adv. Energy Mater. 2012, 2, 710-721.
2. M. D. Slater, D. Kim, E. Lee and C. S. Johnson, Adv. Funct. Mater. 2013, 23, 947-958.
3. L. Wang, Y. Lu, J. Liu, M. Xu, J. Cheng, D. Zhang and J. B. Goodenough, Angew. Chem. Int. Ed. 2013, 52, 1964-1967.
4. V. Palomares, P. Serras, I. Villaluenga, K. B. Hueso, J. Carretero-Gonzalez and T. Rojo, Energy Environ. Sci. 2012, 5, 5884-5901.
5. V. Palomares, M. Casas-Cabanas, E. Castillo-Martinez, M. H. Han and T. Rojo, Energy Environ. Sci. 2013, 6, 2312-2337.
6. H. Pan, Y.-S. Hu and L. Chen, Energy Environ. Sci. 2013, 6, 2338-2360.
7. S. Xin, Y. X. Yin, Y. G. Guo and L. J. Wan, Adv. Mater. 2014, 26, 1261-1265.
8. Y. You, X. L. Wu, Y. X. Yin and Y. G. Guo, Energy Environ. Sci. 2014, 7, 1643-1647.
9. W. Luo, J. Schardt, C. Bommier, B. Wang, J. Razink, J. Simonsen and X. Ji, J. Mater. Chem. A. 2013, 1, 10662-10666.
10. L. Chen, W. Li, Y. Wang, C. Wang and Y. Xia, RSC Adv. 2014, 4, 25369-25373.
11. C. Wadia, P. Albertus and V. Srinivasan, J. Power Sources. 2011, 196, 1593-1598.
12. M. S. Islam and C. A. J. Fisher, Chem. Soc. Rev. 2014, 43, 185-204.
13. M. J. Aragon, C. Vidal-Abarca, P. Lavela and J. L. Tirado, J. Mater. Chem. A. 2013, 1, 13963-13969.
14. V. L. Chevrier and G. Ceder, J. Electrochem. Soc. 2011, 158, A1011-A1014.
15. P. Senguttuvan, G. Rousse, V. Seznec, J.-M. Tarascon and M. R. Palacín, Chem. Mater. 2011, 23, 4109-4111.
16. S. Komaba, W. Murata, T. Ishikawa, N. Yabuuchi, T. Ozeki, T. Nakayama, A. Ogata, K. Gotoh and K. Fujiwara, Adv. Energy Mater. 2011, 21, 3859-3867.
17. C.-M. Park, J.-H. Kim, H. Kim and H.-J. Sohn, Chem. Soc. Rev. 2010, 39, 3115-3141.
18. A. Darwiche, M. T. Sougrati, B. Fraisse, L. Stievano and L. Monconduit, Electrochem. Commun. 2013, 32, 18-21.
19. Y. Wen, K. He, Y. Zhu, F. Han, Y. Xu, I. Matsuda, Y. Ishii, J. Cumings and C. Wang, Nat. Commun. 2014, 5, 4033.
20. L. Baggetto, H.-Y. Hah, J.-C. Jumas, C. E. Johnson, J. A. Johnson, J. K. Keum, C. A. Bridges and G. M. Veith, J. Power Sources, 2014, 267, 329-336.
21. Y. Zhang, J. Xie, T. Zhu, G. Cao, X. Zhao and S. Zhang, J. Power Sources, 2014, 247, 204-212.
22. Y. Zhu, X. Han, Y. Xu, Y. Liu, S. Zheng, K. Xu, L. Hu and C. Wang, ACS Nano, 2013, 7, 6378-6386.

Nanoscale Accepted Manuscript

23. X. L. Wu, Y. G. Guo and L. J. Wan, Chem. - Asian J. 2013, 8, 1948-1958.

24. X. S. Zhou, L. J. Wan and Y. G. Guo, Small, 2013, 9, 2684-2688.

25. W. Luo, S. Lorger, B. Wang, C. Bommier and X. Ji, Chem. Commun. 2014, 50, 5435-5437.

26. L. Ji, M. Gu, Y. Shao, X. Li, M. H. Engelhard, B. W. Arey, W. Wang, Z. Nie, J. Xiao, C. Wang, J.-G. Zhang and J. Liu, Adv. Mater. 2014, 26, 2901-2908.

27. Q. Sun, Q.-Q. Ren, H. Li and Z.-W. Fu, Electrochem. Commun. 2011, 13, 1462-1464.

28. C. Zhu, X. Mu, P. A. van Aken, Y. Yu and J. Maier, Angew. Chem. Int. Ed. 2014, 53, 2152-2156.

29. D. W. Su, S. X. Dou and G. X. Wang, Chem. Commun. 2014, 50, 4192-4195.

30. X. S. Zhou, Z. H. Dai, J. C. Bao and Y. G. Guo, J. Mater. Chem. A. 2013, 1, 13727-13731.

31. H. Kim and J. Cho, Chem. Mater. 2008, 20, 1679-1681.

32. X. Zhou, Z. Dai, J. Bao and Y.-G. Guo, J. Mater. Chem. A. 2013, 1, 13727-13731.

33. L. Baggetto, H.-Y. Hah, C. E. Johnson, C. A. Bridges, J. A. Johnson and G. M. Veith, Phys. Chem. Chem. Phys. 2014, 16, 9538-9545.

34. I. T. Kim, E. Allcorn and A. Manthiram, Phys. Chem. Chem. Phys. 2014, 16, 12884-12889.

35. B. Farbod, K. Cui, W. P. Kalisvaart, M. Kupsta, B. Zahiri, A. Kohandehghan, E. M. Lotfabad, Z. Li, E. J. Luber and D. Mitlin, ACS Nano, 2014, 8, 4415-4429.

36. J. F. Qian, Y. Chen, L. Wu, Y. L. Cao, X. P. Ai and H. X. Yang, Chem. Commun. 2012, 48, 7070-7072.

37. D. Y. W. Yu, P. V. Prikhodchenko, C. W. Mason, S. K. Batabyal, J. Gun, S. Sladkevich, A. G. Medvedev and O. Lev, Nat. Commun. 2013, 4.

38. P. Nie, L. Shen, H. Luo, H. Li, G. Xu and X. Zhang, Nanoscale, 2013, 5, 11087-11093.

39. P. Nie, L. Shen, H. Luo, B. Ding, G. Xu, J. Wang and X. Zhang, J. Mater. Chem. A. 2014, 2, 5852-5857.

40. Y. Wang, H. Li, P. He, E. Hosono and H. Zhou, Nanoscale, 2010, 2, 1294-1305.

41. J. Ma, X. Duan, J. Lian, T. Kim, P. Peng, X. Liu, Z. Liu, H. Li and W. Zheng, Chem. - Eur. J. 2010, 16, 13210-13217.

42. P. Nie, L. Shen, F. Zhang, L. Chen, H. Deng and X. Zhang, CrystEngComm, 2012, 14, 4284-4288.

Nanoscale Accepted Manuscript